Neoplasia • Vol. 7, No. 5, May 2005, pp. 528–536 528

www.neoplasia.com

Tumor Vessel Compression Hinders Perfusion of Ultrasonographic Contrast Agents[1]

Mirco Galiè, Mirko D'Onofrio†, Maura Montani‡, Augusto Amici‡, Laura Calderan*, Pasquina Marzola*, Donatella Benati*, Flavia Merigo*, Cristina Marchini‡ and Andrea Sbarbati**

*Section of Anatomy and Histology, Department of Morphological and Biomedical Sciences, University of Verona, Verona (VR), Italy; †Section of Radiology, Department of Morphological and Biomedical Sciences, University of Verona, Verona (VR), Italy; ‡Genetic Immunization Laboratory, Department of Molecular, Cellular, and Animal Biology, University of Camerino, Camerino (MC), Italy

Abstract

Contrast-enhanced ultrasound (CEUS) is an advanced approach to *in vivo* assessment of tumor vascularity and is being increasingly adopted in clinical oncology. It is based on 1– to 10 μm–sized gas microbubbles, which can cross the capillary beds of the lungs and are effective echo enhancers. It is known that high cell density, high transendothelial fluid exchange, and poorly functioning lymphatic circulation all provoke solid stress, which compresses vessels and drastically reduces tumor blood flow. Given their size, we supposed that the perfusion of microbubbles is affected by anatomic features of tumor vessels more than are contrast agents traditionally used in dynamic contrast-enhanced magnetic resonance imaging (DCE-MRI). Here, we compared dynamic information obtained from CEUS and DCE-MRI on two experimental tumor models exhibiting notable differences in vessel anatomy. We found that tumors with small, flattened vessels show a much higher resistance to microbubble perfusion than to MRI contrast agents, and appear scarcely vascularized at CEUS examination, despite vessel volume adequate for normal function. Thus, whereas CEUS alone could induce incorrect diagnosis when tumors have small or collapsed vessels, integrated analysis using CEUS and DCE-MRI allows *in vivo* identification of tumors with a vascular profile frequently associated with malignant phenotypes.

Neoplasia (2005) **7,** 528–536

Keywords: CEUS, DCE-MRI, transgenic mice, mammary tumor, tumor blood flow.

Introduction

Tumor vascularization is strongly correlated to histologic grade, and much interest has been devoted to its noninvasive investigation *in vivo*.

Dynamic contrast-enhanced magnetic resonance imaging (DCE-MRI) techniques are widely used in preclinical and clinical settings [1–3].

Contrast media for ultrasonography (UCAs) have recently been developed, providing exciting new opportunities for functional ultrasound imaging [4–6]. They are composed of 1– to 10 μm–sized microbubbles, which can cross capillary beds and are safe and effective echo enhancers. Given their micrometer size, microbubbles should simulate the dynamics of erythrocytes because they are able to flow through macrocirculation and microcirculation without extravasation from the vascular network, despite the leakiness of tumor vessels. Some studies provided preliminary evidence that microbubble-induced enhancement could be useful in tumor diagnosis [7–9].

In clinical practice, CEUS-based analysis of *tumor vascularization* is based on the intensity of contrast agent–induced signal enhancement. This parameter is assumed to be proportionate to total vascular volume, but how much it may be affected by the anatomic and functional characteristics of tumor vessels and their surrounding parenchyma is far from obvious.

It has been reported that frequently occurring aspects of tumor anatomy such as high cell density [10], high transendothelial fluid exchange [11,12], and poorly functioning lymphatic circulation [13–16] all provoke solid stress, which can compress vessels and drastically reduce tumor blood flow.

Due to their size, it is reasonable to suppose that the perfusion of microbubbles could be more affected by tumor histologic and vascular architecture than are the micromolecular and even macromolecular contrast agents commonly used in DCE-MRI. Clarification of this question would be of notable interest because it would highlight the risk of diagnostic mistakes in the clinical use of microbubbles. Furthermore, the integration of CEUS and DCE-MRI technologies would

Address all correspondence to: Mirco Galiè, Section of Anatomy and Histology, Department of Morphological and Biomedical Sciences, University of Verona, Strada Le Grazie 8, Verona 37134, Italy. E-mail: mirco@anatomy.univr.it

[1]Grant sponsor: Fondazione Cassa di Risparmio di Verona (Bando 2001 "Ambiente e sviluppo sostenibile").

Received 18 November 2004; Revised 3 January 2005; Accepted 4 January 2005.

DOI 10.1593/neo.04730

make it possible to obtain more information than a generic vascularity index.

With the aim of investigating how the histologic features of tumor vessels and the surrounding parenchyma can affect CEUS- and DCE-MRI–based vascular diagnosis, we compared the application of these technologies to an experimental model of carcinoma and an experimental model of sarcoma, both provoked by subcutaneous injection of different cell lines that had been established from the same mammary carcinoma model. These two histotypes of tumors were chosen because they exhibited a different vascular anatomy, as described below. As the carcinomatoid one, the sarcomatoid model represents a tumor histotype that frequently occurs in humans. Sarcomas can be observed in varied anatomic districts, including the breasts [17–20], where they are the result of an aberrant stromal reactivity [21–23] and/or epithelial mesenchymal transition event [24].

Materials and Methods

Animals

This study was carried out on FVB mice, line 233, which were transgenic for the activated isoform of rat HER-2/neu oncogene (FVB/neuNT233), purchased from Charles River Laboratories (Calco, Italy). The mice had been bred under "pathogen-free" conditions inside galvanized cages (four to six mice per cage) at 20 ± 1°C temperature and 50 ± 1% humidity. The animals were exposed to cycles of 12 hours light/12 hours dark, and were fed with standard foodstuff (Nossen, UD, Italy) and water *ad libitum*. The presence of transgene was routinely checked by polymerase chain reaction on tail DNA using primers specific for vector (sense: 5′-ATCGGTGATGTCGGCGATAT-3′) and MMTV promoter (antisense: 5′-GTAACACAGGCAGATGTAGG-3′) sequences.

Establishment of Transgenic Mammary Carcinoma Cell Cultures

Tumors surgically excised from 6-month–old transgenic mice were minced with scissors and lancet, seeded in tissue culture flasks in Dulbecco's modified essential medium (DMEM) + 20% fetal bovine serum (FBS) (Invitrogen, Carlsbad, CA, USA), and incubated at 37°C in a humidified 5% CO_2 atmosphere. After the sprouting of cells from tissue fragments, the cultures were periodically washed briefly (1–3 minutes) with trypsin–EDTA to detach contaminating fibroblasts without damage to epithelial areas. After several washings, 3 to 5 months after plating, the resulting confluent epithelial monolayer was diluted to as few as 5 cells/ml and split in a 96-well plate to obtain clones derived from single cells. The colonies were subsequently subcloned and the cell lines obtained were established by several subculturing steps.

Experimental Tumors

A total of 5×10^5 cells suspended in 0.1 ml of phosphate-buffered saline (PBS) was subcutaneously injected into the backs of 5– to 7 week–old female FVB/neuNT233 mice. Tumor growth was followed and tumor size was measured weekly using calipers. The animals underwent DCE-MRI and CEUS when the longest diameter of their tumors reached 10 to 15 mm.

DCE-MRI with Gd-DTPA-Albumin

Six animals that had been subcutaneously injected with the A17 cell line and six animals injected with the BB1 cell line underwent DCE-MRI exams using Gd-DTPA-albumin (obtained from R. Brasch, Contrast Media Laboratory, University of California, San Francisco, CA) as the contrast agent.

The animals were anesthesized by inhalation of a mixture of air and O_2, which contained 0.5% to 1% halothane, and were placed in a prone position inside a 3.5-cm i.d. transmitter–receiver birdcage coil. Images were acquired using a Biospec tomograph (Burker, Karlsruhe, Germany) equipped with a 4.7-T, 33-cm bore horizontal magnet (Oxford Ltd., Oxford, UK). Coronal spin-echo (SE) and transversal multislice, fast SE T2w (RARE, TE = 70 milliseconds) images were acquired for tumor localization. Afterward, a dynamic series of 3D transversal spoiled-gradient echo (SPGR) images was acquired with the following parameters: repetition time (TR)/echo time (TE) = 50/3.5 milliseconds, flip angle (α) = 90°, matrix size = $128 \times 64 \times 32$, and field of view (FOV) = $5 \times 2.5 \times 3$ cm^3 (corresponding to 0.39×0.39 mm^2 in-plane resolution and 0.94 mm slice thickness), The number of acquisitions (NEX) = 1. The acquisition time for a single 3D image was 104 seconds; a dynamic scan of 24 images was acquired with 30-second intervals between each image (total acquisition time, 53 minutes). The contrast agent was injected in bolus during the interval between the first and the second scan. A phantom containing 1 mM Gd-DTPA in saline was inserted in the FOV and used as an external reference standard to normalize possible spectrometer drifts during the acquisition [25]. The experimental protocol closely followed that previously described by Daldrup et al. [25] except that precontrast T_1 values were measured using the IR-SnapShot Flash technique [26].

Data analysis was adapted from references for the special case of macromolecular contrast agents. Briefly, the signal intensity was firstly converted to Gd concentration; the time dependence of Gd concentration was analyzed in terms of a two-compartment tissue model composed of plasma and interstitial water equilibrating pools. Fitting of the theoretical expression to experimental data provided quantitative values of transendothelial permeability (kPS) and fractional plasma volume (fPV) of the tumor tissue. Images were analyzed on a region of interest (ROI) basis to obtain the average value of kPS and fPV in the selected ROI: in each animal, the central five slices of the 3D data set were analyzed. For each considered slice, ROIs were manually tracked to cover the tumor. The signal was averaged and analyzed to obtain the mean kPS and fPV values of the selected slice.

CEUS

All the CEUS examinations were performed on a Technos (Esaote, Milan, Italy) with harmonic microbubble-specific

imaging setting at very low acoustic ultrasound pressure (CnTI, 8 MHz; MI < 0.1; DP 15 kPS). Sulfur hexafluoride in the form of microbubbles (SonoVue Bracco, Milan, Italy) was used. A linear array transducer (LA532E 8-3) was held over the tumor after gel was applied to the skin overlying the tumor. A bolus injection (0.01–0.05 ml) of contrast medium was administered into a tail vein catheter.

Six animals subcutaneously injected with the A17 cell line and six animals injected with the BB1 cell line underwent CEUS examination. The dynamic enhancement of the tumor was observed in real time and continuously recorded over a period of 180 seconds.

The curves of enhancement (time–intensity curves) of A17 and BB1 tumors were obtained using IMAGELAB software (Esaote) by locating an ROI over the tumors and were analyzed based on the following parameters:

1) Maximal intensity (Mi): signal intensity of the maximal peak of the curve in arbitrary units.

2) Slope (*S*): parameter automatically calculated by Technos software, in arbitrary units based on the ratio between Mi and time-to-peak.

3) Wash-out (Wo): percentage decrease of signal intensity between Mi and Fi. It is quantified by means of the following calculation: $[(Mi - Fi)/Mi] \times 100$.

4) Final intensity (Fi): signal intensity at the final time of acquisition (185 seconds).

When the curve rose continuously after the initial upstroke, Mi was taken to be the signal intensity at the endpoint of acquisition (180 seconds), whereas *S* and Wo were assumed to be zero.

DCE-MRI with Gd-DTPA

With the aim of confirming the vascular differences between tumor histotypes observed by means of DCE-MRI with macromolecular contrast agent (Gd-DTPA-albumin), two animals per histotype group underwent DCE-MRI with Gd-DTPA (MAGNEVIST, Schoering, Germany) as contrast agent, within the 24 hours prior to CEUS examination. After coronal SE and transversal multislice, fast SE T2-weighted (RARE; TE_{eff} = 70 milliseconds) images were acquired for tumor localization, a dynamic series of T1-weighted, spoiled GRE images was acquired with the following parameters: TR = 65 milliseconds, TE = 3.8 milliseconds, $\alpha = 90°$, matrix size = 128 × 64 zero filled at 256 × 256, FOV = 5 × 2.5 cm^2, and space resolution = 391 × 391 μm^2. A single slice (slice thickness = 1.5 mm) was acquired at the tumor center. The acquisition time for a single image was 4.1 seconds and there was an interval of 1 second between successive images (time resolution = 5.1). A total of 60 images was acquired, 3 before and 57 after the contrast medium bolus injection; Gd-DTPA at a 100-μmol/kg dosage was used. The dynamic evolution of the signal was observed for about 5 minutes.

Histologic and Immunohistochemical Evaluation

The tumors of sacrificed mice were removed and processed for ultrastructural and light microscopy evaluation. For histology and immunohistochemistry, the tumors were fixed in zinc fixative, dehydrated, transversally cut in half, and embedded in paraffin wax. The two halves were blocked and processed separately, with the cut edge ultimately facing the microtome surface. Two consecutive sections were taken from the face of each block and then additional sections were taken at intervals of 100 μm as far as roughly 1 mm into each block. Sections (5 μm) were cut on a rotary microtome and placed on polylysine-coated slides. The sections obtained were in planes corresponding approximately to those utilized in MRI and US evaluations. For histologic analysis, they were stained using hematoxylin–eosin. Endothelial cells were identified by immunohistochemical staining for platelet endothelial cell adhesion molecule-1 (PECAM-1 or CD31), using a rat monoclonal antibody directed against mouse CD31 (Pharmingen, San Diego, CA). For immunoperoxidase staining, sections were incubated in 3% hydrogen peroxide to block endogenous peroxidase activity. To prevent aspecific antibody binding, sections were preincubated for 20 minutes in PBS, pH 7.4, containing 10% normal rabbit serum. Next, sections were incubated overnight at 4°C with the primary antibody directed against CD31 (dilution of 1:100). Sections were rinsed for 15 minutes with PBS, followed by incubation with biotinylated secondary antibody for 45 minutes at room temperature. After washing with PBS, the bound antibody was visualized by the peroxidase ABC method using diaminobenzidine (Sigma Chemical Co., St. Louis, MO) as the developer. The sections were rinsed with distilled water and mounted in aqueous solutions. For the above immunohistochemical procedures, controls were performed by replacing the primary antibody with 10% nonimmune serum. Further controls were made by omitting the secondary antibody. Controls were always negative. Three samples for each histotype underwent vessel counting at ×20 magnification in a 0.180-mm^2 field. For each sample, five fields along the longest diameter and five along the shortest diameter of the tumor slice were chosen. Fields overlapping necrotic areas were excluded.

Ultrastructural Analysis

For ultrastructural evaluation, part of the tumors was fixed in 2.5% glutaraldehyde in Sorensen buffer for 2 hours, postfixed in 1% osmium tetroxide for 1 hour, dehydrated in graded ethanol, embedded in epon-araldite, and cut with an Ultracut E apparatus (Reichert, Wien, Austria). The semithin sections were stained with toluidine blue. The ultrathin sections were stained with lead citrate and uranyl acetate and observed with an EM10 electron microscope (Zeiss, Oberkocken, Germany).

Statistical Analysis

MANOVA was used to evaluate the statistical significance of the differences between A17 and BB1 tumors regarding the following parameters:

1) kPS
2) fPV
3) vessel count

4) vessel area
5) Mi
6) *S*
7) Wo.

$P < .05$ was accepted as statistically significant.

Results

Cell Lines and Tumors

From primary mammary tumors excised from 7– to 8-month–old transgenic mice, we established two cell lines that exhibited different morphologic features.

The BB1 cell culture was formed of rounded cells with typical epithelial morphology, which grew in clusters of cells with tight junctions (Figure 1*A*).

The A17 culture was composed of large star- or spindle-shaped cells forming homogeneous layers on cell culture plates as well as on Petri dishes (Figure 1*B*). On prolonged culture at confluence, the A17 cells formed foci in which the cells grew on top of each other, a phenotype typical of transformed cells.

When subcutaneously injected into the backs of animals, the BB1 cells grew, after a short latency period, into tumors that appeared as unifocal masses composed of one or more lobes. Histologic analysis showed the features of a lobular carcinoma as very similar to the transgenic parental tumor. The tumor parenchyma was formed of round to polygonal cells, and was rich in edema and hemorrhagic areas (Figure 1, *C* and *D*).

The subcutaneous injection of A17 cells led to highly invasive sarcomatoid-like tumors formed of spindle-shaped or polygonal neoplastic cells (Figure 1*E*). In A17 tumor parenchyma, necrotic areas were not observed.

At T2-weighted MRI, A17 tumors showed more homogeneous and notably brighter parenchyma than BB1 tumors

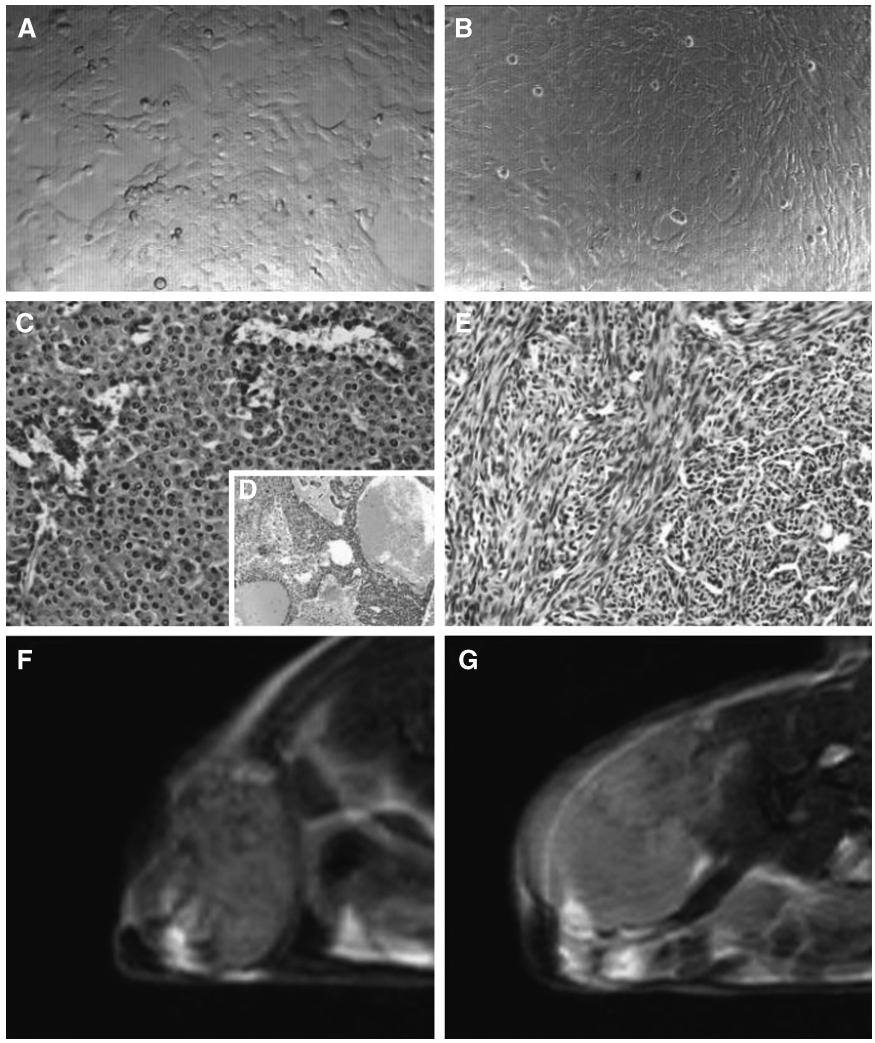

Figure 1. *Morphologic differences between BB1 and A17 tumor histotypes. Two different cell lines were established from mammary tumors, which had spontaneously arisen in FVB/neuNT233 transgenic mice. The BB1 cells exhibited a round to polygonal shape, and grew in tightly junctioned clusters (A). The A17 cells were star- or spindle-shaped and grew in monolayers free of growth constraints (B). The subcutaneous injection of BB1 cells provoked lobular carcinomas resembling spontaneous tumors (C), with large hemorrhagic areas (D), whereas A17 cells generated sarcomatoid lesions (E). At T2-weighted MRI, BB1 parenchyma showed a heterogeneous and notably lower signal intensity than A17 tumors (F and G).*

Table 1. Quantitative Analysis of Vascular Parameters Obtained by DCE-MRI, CEUS, and CD31 Immunostaining.

	DCE-MRI		CEUS			CD31	
	Mean fPV (ml/cm^3 tissue)	Mean kPS [$(ml/min)/cm^3$ tissue]	Mean Mi (a.u.)	Mean *S* (a.u.)	Mean Wo (%)	Mean Vessel Count	Mean Vessel Size (m^2)
A17	0.031 ± 0.02	0.00081 ± 0.00045	0.087 ± 0.033	0.00057 ± 0.00052	13.60 ± 15.18	165.53 ± 42.04	183.82 ± 41.80
BB1	0.013 ± 0.01	0.00040 ± 0.00036	0.18 ± 0.043	0.0036 ± 0.0016	36.32 ± 24.39	79.07 ± 31.88	465.56 ± 249.11
Statistical significance	***P* = .00001**	***P* = .0008**	***P* = .002**	***P* = .002**	*P* = .08	*P* ~ **.000**	*P* ~ **.000**

Mean values ± SD for each vascular parameter were obtained by the analyses of DCE-MRI, CEUS, and CD31 immunostaining data.
Mi and *S* values are expressed in arbitrary units (a.u.). In vessel count, fields overlapping necrotic areas were excluded.
The necrotic fraction represented 30% to 40% of BB1 tumors, which was undetectable in A17 tumors.
For each parameter, a comparison was made between the two histotypes and the statistical significance of any difference was reported.
P values accepted as statistically significant are in bold face.

(Figure 1*F*), suggesting a high cellular density and/or a high level of hydration [27].

Vascular Analysis

The vascularity of the two different tumor histotypes was comparatively evaluated by immunocytochemical, DCE-MRI, and CEUS analyses. Quantitative data and their statistical significance are reported in Table 1.

Morphologic and Quantitative Analyses of Vessels

Histologic analysis of CD31-immunostained tumor slices showed that the anatomic organization of the vasculature was different in the two histotypes.

Considering the viable areas, the vessels of A17 tumors (Figure 2, *A* and *B*) were, on average, significantly more numerous and smaller than those in BB1 tumors (Figure 2*C*), and were homogeneously spread through the tumor paren-

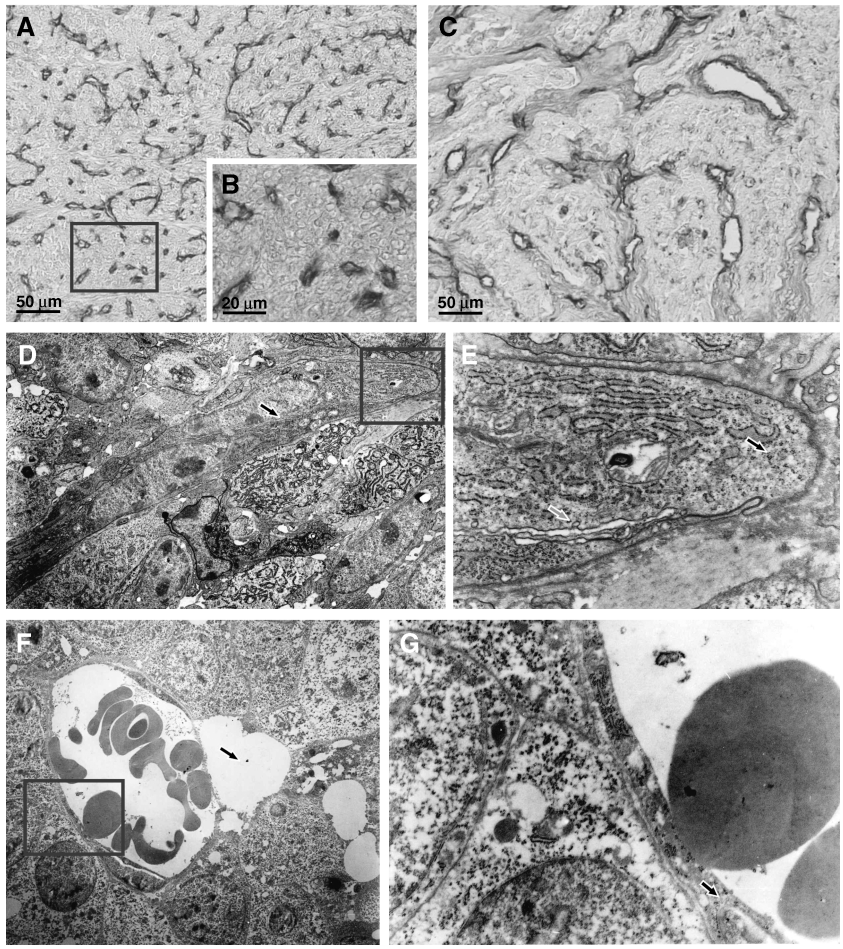

Figure 2. *Postmortem histopathologic analysis of BB1 and A17 tumor vasculature. Postmortem analysis of CD31-immunostained sections showed that A17 vasculature was composed of extremely numerous but, on average, very small vessels (A and B). The vessels of BB1 tumors proved less numerous and, on average, larger, and were confined within the stromal compartment of viable areas (C). At ultrastructural analysis, the lumina of A17 vessels frequently appeared flattened (D; arrow) and the endothelial cells exhibited blastic traits such as abundance of polyribosomes (E; black filled arrow). The occurrence of pinocytotic vesicles (E; gray filled arrow) suggests that vessel lumina were functional. In contrast, at ultrastructural analysis, the vessels of BB1 tumors frequently appeared enlarged (F), occasionally close to perivascular edemas (F; arrow) and delimited by morphologically differentiated endothelial cells (G; arrow).*

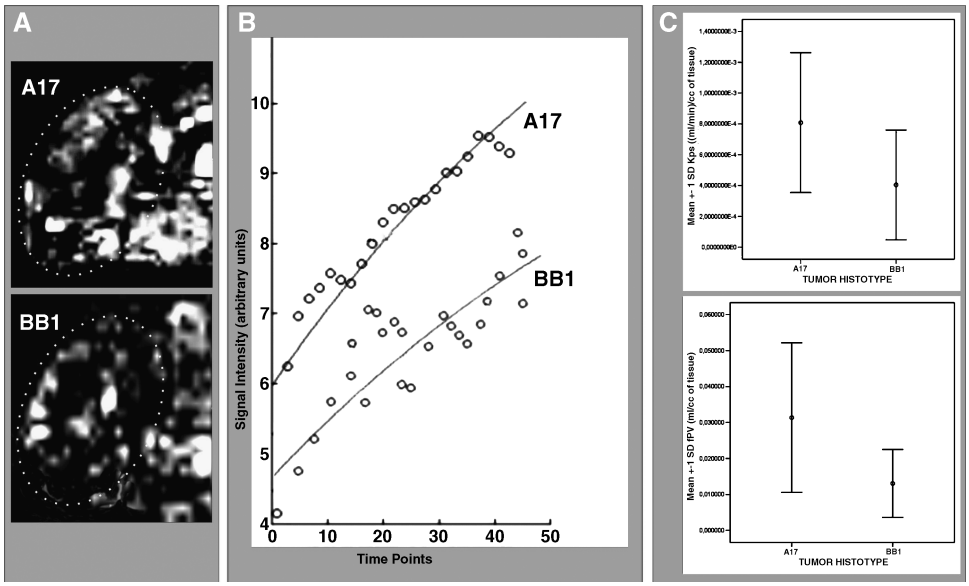

Figure 3. *In vivo assessment of BB1 and A17 tumor vasculature by DCE-MRI with Gd-DTPA-albumin. A series of quadrangular ROIs matching the whole tumor section was manually selected on the MRI images (A), and was analyzed as previously described [20] to measure the fractional vascular volume (fPV) and transendothelial permeability (kPS) of tumor vessels. The first parameter is dependent on the intercept between the curve and the y-axis; the latter depends on the slope of the curve (B). Both parameters proved significantly higher, on average, in A17 than in BB1 tumors (C; see also Table 1).*

chyma. BB1 vessels, less numerous and on average larger, proved to be confined to the stromal compartment of viable areas. The difference in number was complementary to differences in size, so that the total vascular volume of the two tumor histotypes was comparable (Table 1). However, given that a notable fraction of BB1 parenchyma was necrotic, and considering the whole tumor sections, A17 tumors proved notably more vascularized than BB1 tumors.

At ultrastructural examination, most A17 vessels showed small lumens, often flattened by hypertrophic endothelial cells, and exhibited evident blastic traits such as numerous organelles, in particular free or endoplasmic reticulum–associated polyribosomes, and a high cytoplasm/nucleus ratio. The metabolic activity of endothelial cells and the functionality of vessel lumina were confirmed by the presence of pinocytotic vesicles near the plasmalemma of endothelial cells (Figure 2, *D* and *E*). The BB1 tumors' ultrastructure showed enlarged vessels, frequently lined by differentiated endothelial cells (Figure 2, *F* and *G*).

Gd-DTPA-Albumin DCE-MRI Analysis

Contrast-enhanced MRI performed by injecting Gd-DTPA-albumin was used with the aim of quantitatively evaluating the vascularity of A17 and BB1 tumors (Figure 3). Following a previously published protocol [28], we analyzed the two tumor histotypes for two vascular parameters: fractional plasma volume (fPV) and endothelial transfer coefficient (kPS). fPV is measured as the signal intensity increase immediately after contrast agent injection. The parenchyma of the A17 tumors showed a significantly higher fPV than the BB1 tumors (Figure 3*C* and Table 1).

The kPS parameter is calculated based on the kinetic increase of signal intensity after contrast agent injection and is a measure of transendothelial permeability. It proved significantly higher in the A17 tumors than in BB1 tumors (Figure 3*C* and Table 1).

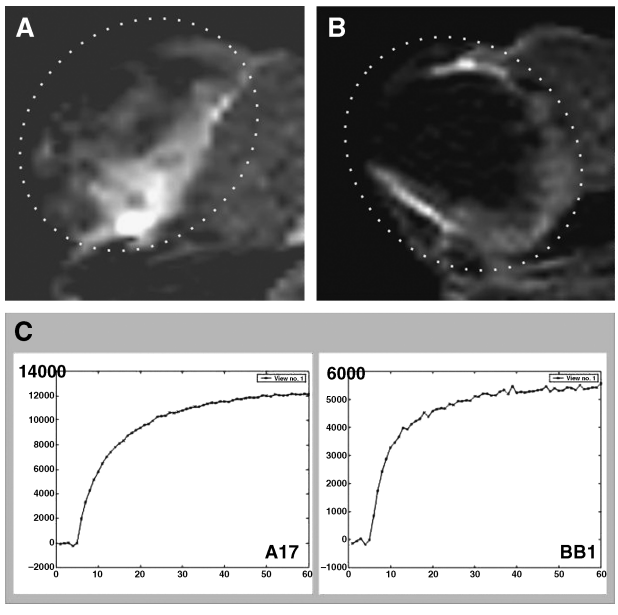

Figure 4. *In vivo assessment of BB1 and A17 tumor vasculature by DCE-MRI with Gd-DTPA. DCE-MRI with Gd-DTPA as contrast agent confirmed that A17 tumors showed a higher level of vascularization than BB1 tumors. Unlike DCE-MRI with Gd-DTPA-albumin, the maps of enhancement obtained by pixel-by-pixel subtraction between the last postcontrast and the precontrast images make evident the difference in size and the distribution of vessel network between A17 (A) and BB1 (B) tumors. Two representative time–intensity curves show vascular differences observed between the two tumor histotypes (C).*

Gd-DTPA DCE-MRI Analysis

Two mice per histologic group underwent DCE-MRI examination with Gd-DTPA as the contrast agent (Figure 4).

As expected, the curves of enhancement of A17 tumors followed a signal intensity value scale, which was notably higher than that of BB1 tumors (Figure 4*C*).

CEUS

DCE ultrasound performed using SonoVue microbubbles as the contrast agent proved apparently inconsistent with DCE-MRI observations (Figure 5). The Mi and *S* values of BB1 tumors were, on average, significantly higher than those of A17 tumors. Time–intensity curves of BB1 tumors had a mean Wo that was almost three times higher than those of A17 tumors, and two cases of A17 curves showed a continuous time increase in signal intensity. However, at statistical analysis, the Wo values of BB1 and A17 tumors were not significantly ($P < .08$) different (Figure 5*C* and Table 1).

Discussion

Our data demonstrate that particular histologic features can lead to a mismatch between DCE-MRI and CEUS. DCE-MRI, as well as immunohistochemical analysis, showed that carcinosarcomatoid lesions (A17 tumors) were richer in vessels than carcinomas (BB1 tumors), but the first histologic type of tumor exhibited a significantly higher resistance to microbubble flow and a time–intensity dynamic characterized by lower Mi, delayed *S*, and reduced Wo.

The histologic and ultrastructural analysis of tumor samples provided a reasonable explanation for this mismatch. In accordance with MRI-based measurements of vascular parameters, A17 tumors had a notably large number of vessels homogeneously spread within tumor parenchyma, but their lumina often appeared to have diameters on the order of a few micrometers, and many of them seemed to have collapsed under the pressure exerted by the surrounding high cellular density. It has recently been demonstrated that solid stress generated by tumor cells growing in a confined space compresses blood vessels and increases microvascular pressure (MVP) and interstitial fluid pressure (IFP), whereas reduction in cell density caused by drug-induced apoptosis can decompress vessels and restore normal blood flow [10]. BB1 tumor parenchyma showed an evident abundance of large and small necrotic areas, which probably keep solid stress levels low and allow vessels to remain open.

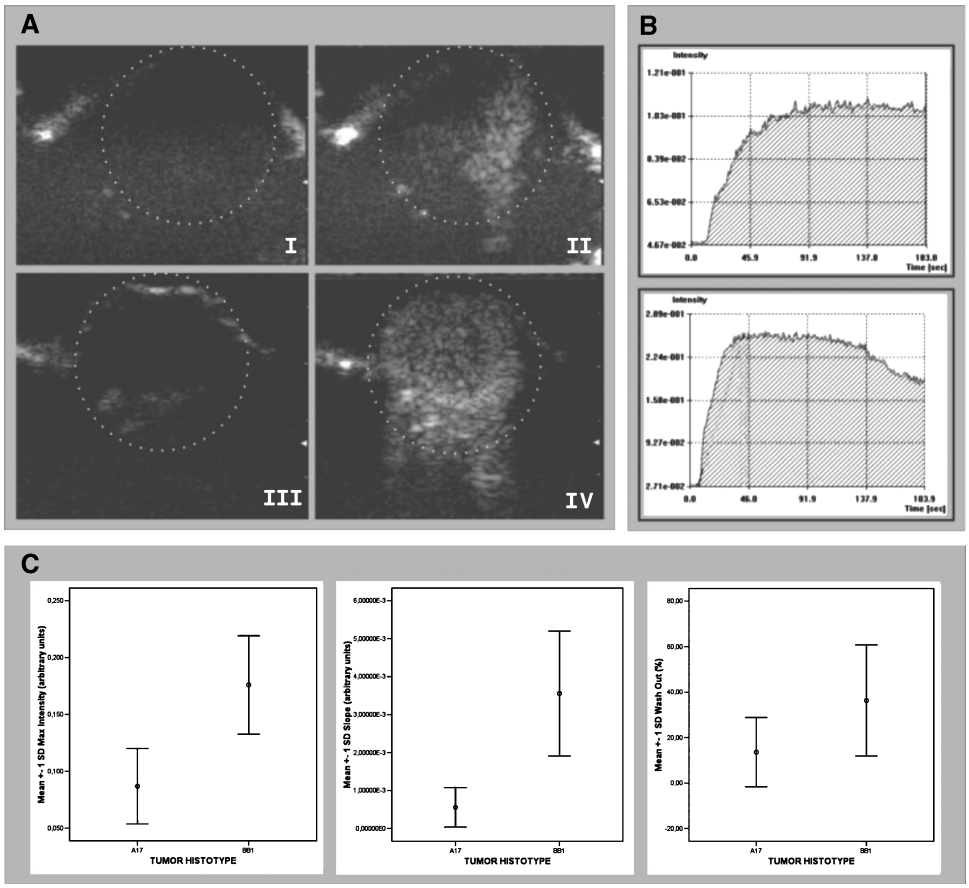

Figure 5. *In vivo assessment of BB1 and A17 tumor vasculature by CEUS with SonoVue contrast agent. CEUS showed that A17 tumors had a lower level of vascularization than BB1 tumors. Signal enhancement after contrast agent injection was less evident in A17 (A, I: precontrast; II: postcontrast) than in BB1 (A, III: precontrast; IV: postcontrast) tumors. Two representative time–intensity curves show differences between time course contrast enhancement observed in A17 (B, top panel) and BB1 (B, bottom panel) tumors. BB1 tumors had a reduced maximal intensity peak (Mi), delayed slope (S), and reduced wash-out (Wo) in comparison with BB1 tumors (C; see also Table 1).*

The high transendothelial permeability (kPS) of A17 vessels could also contribute to solid stress exerted by tumor parenchyma on vessels. An enhanced fluid exchange across leaky endothelial walls can shift the hydrostatic equilibrium between the microvascular and interstitial space toward a state of interstitial hypertension.

In normal tissue, extravasation of fluid from the vessel bed is tightly regulated due to the low hydraulic conductivity and the highly specialized selectivity of vascular walls. The small amount of any extravasated fluid is readily drained by lymphatic vessels. Under these conditions, the hydrostatic pressure gradient between the vascular and interstitial compartments is kept stable and, hence, the IFP is close to zero. Enhanced transendothelial permeability, in the absence of a functioning lymphatic system, may cause a potential coupling between vascular and interstitial fluid flow, which in turn leads to peritumoral edema and IFP enhancement [11,12,29].

A high density of newly sprouted, small-sized, leaky, morphologically immature vessels in tumors can be the consequence of intense neoangiogenesis. Continuous and vigorous stimulus to the proliferation of endothelial cells in tumors, estimated to be 50 to 200 times greater than that of endothelial cells in normal tissue [30,31], is frequently not supported by a coordinated maturation program [32] and has been reported to be associated with poor prognosis [33].

In our study, A17 vessels showed blastic traits that were typical of newly formed vessels. They appeared less mature, as well as more numerous and homogeneously distributed than BB1 vessels, which exhibited a notably large mean diameter reported to be typical of carcinomas [34].

However, resistance to microbubble flow is not necessarily a sign of poorly functional vascularization. Their notable growth rate, high invasive potential, absence of necrotic areas, and frequent occurrence of pinocytotic vesicles in the cytoplasm of endothelial cells all suggested that A17 tumors were endowed with an efficient vascular system. Small-sized or flattened vessels might trap or break air microbubbles, but still be functional for the flow of erythrocytes, which have high deformability and resistance to pressure. This may explain their refractoriness to wash-in (delayed *S* and low Mi) and their reduced wash-out. However, it is possible that a portion of A17 tumor microcirculation could be functionally impervious to microbubbles as well as erythrocytes. It is known that in physiological conditions, a small proportion of functionally opened capillaries provides sufficient blood perfusion for the needs of tissues, whereas blood hyperflow could even be harmful.

In our experimental model, the mismatch between CEUS and DCE-MRI time course parameters was observed in carcinosarcomatoid lesions provoked by the subcutaneous injection of mesenchymal-like cells of mammary origin. Thus, in mammary tumor analysis, this mismatch could give rise to suspicious epithelial–mesenchymal transition [35].

Taken together, these observations demonstrate that CEUS alone could induce incorrect diagnoses when tumors have particular morphologic features such as small, collapsed vessels, but integrated analysis using CEUS and DCE-MRI makes it possible to identify *in vivo* tumors characterized by numerous but phenotypically immature vessels: a typical consequence of an intense neoangiogenesis.

Further investigations are needed to compare the informative potential of CEUS with that of other *in vivo* methods of vascular analysis. An interesting insight would be to verify whether the tumor size can affect CEUS- and MRI-based diagnosis. In the present work, we employed 10- to 15-mm specimens—consistent with the fact that, in breast cancer, diagnostic problem arises in the size of such nodules. Yet, as the tumor size enlarges, necrotic areas and vascular collapse might change and the CEUS and MRI analyses might be differently affected.

References

[1] Kuhl CK, Mielcareck P, Klaschik S, Leutner C, Wardelmann E, Gieseke J, and Schild HH (1999). Dynamic breast MR imaging: are signal intensity time course data useful for differential diagnosis of enhancing lesions? *Radiology* **211,** 101–110.

[2] Brasch RC, Li KC, Husband JE, Keogan MT, Neeman M, Padhani AR, Shames D, and Turetschek K (2000). *In vivo* monitoring of tumor angiogenesis with MR imaging. *Acad Radiol* **7,** 812–823.

[3] Daldrup-Link HE and Brasch RC (2003). Macromolecular contrast agents for MR mammography: current status. *Eur Radiol* **13,** 354–365.

[4] Harvey CJ, Blomley MJ, Eckersley RJ, and Cosgrove DO (2001). Development in ultrasound contrast media. *Eur Radiol* **11,** 675–689.

[5] Blomley MJ, Cooke JC, Unger EC, Monaghan MJ, and Cosgrove DO (2001). Microbubble contrast agents: a new era in ultrasound. *Br Med J* **19,** 1222–1225.

[6] Blomley MJ and Eckersly RJ (2002). Functional ultrasound methods in oncological imaging. *Eur J Cancer* **38,** 2108–2115.

[7] Kedar RP, Cosgrove D, McCready VR, Bamber JC, and Carter ER (1996). Microbubble contrast agent for color Doppler US: effect on breast masses. Work in progress. *Radiology* **198,** 679–686.

[8] D'Onofrio M, Mansueto G, Falconi M, and Procacci C (2004). Neuroendocrine pancreatic tumor: value of contrast enhanced ultrasonography. *Abdom Imaging* **29,** 246–258.

[9] D'Onofrio M, Rozzanigo U, Caffarri S, Zogno A, and Procacci C (2004). Contrast-enhanced US of hepatocellular carcinoma. *Radiol Med (Torino)* **107,** 293–303.

[10] Griffon-Etienne G, Boucher Y, Brekken C, Suit HD, and Jain RK (1999). Taxane-induced apoptosis decompresses blood vessels and lowers interstitial fluid pressure in solid tumors: clinical implications. *Cancer Res* **59,** 3776–3782.

[11] Sevick EM and Jain RK (1999). Measurement of capillary filtration coefficient in a solid tumor. *Cancer Res* **51,** 1352–1355.

[12] Baish JW, Netti PA, and Jain RK (1997). Transmural coupling of fluid flow in microcirculatory network and interstitium in tumors. *Microvasc Res* **53,** 128–141.

[13] Boucher Y and Jain RK (1992). Microvascular pressure is the principal driving force for interstitial hypertension in solid tumors: implications for vascular collapse. *Cancer Res* **52,** 5110–5114.

[14] Baxter LT and Jain RK (1989). Transport of fluid and macromolecules in tumors: I. Role of interstitial pressure and convection. *Microvasc Res* **37,** 77–104.

[15] Leu AJ, Berk DA, Lymboussaki A, Alitalo K, and Jain RK (2000). Absence of functional lymphatics within a murine sarcoma: a molecular and functional evaluation. *Cancer Res* **60,** 4324–4327.

[16] Carmeliet P and Jain RK (2000). Angiogenesis in cancer and other diseases. *Nature* **407,** 257–259.

[17] Sl-Nafussi A (1999). Spindle cell tumours of the breast: practical approach to diagnosis. *Histopathology* **35,** 1–3.

[18] Foschini MP, Dina RE, and Eusebi V (1993). Sarcomatoid neoplasms of the breast: proposed definitions for biphasic and monophasic sarcomatoid mammary carcinomas. *Semin Diagn Pathol* **10,** 128–136.

[19] Ostrowski JL, Horgan K, Krausz T, and Quinn CM (1998). Monophasic sarcomatoid carcinoma of the breast. *Histopathology* **32,** 184–186.

[20] Fisher C (2004). Myofibrosarcoma. *Virchows Arch* **445,** 215–223.

[21] Rønnov-Jessen L, Petersen OW, and Bissel MJ (1996). Cellular

changes involved in conversion of normal to malignant breast: the importance of the stromal reaction. *Physiol Rev* **76,** 69–125.
[22] Petersen OW, Nielsen HL, Gudjonsson T, Villadsen R, Rønnov-Jessen L, and Bissel MJ (2001). The plasticity of human breast carcinoma cells is more than epithelial to mesenchymal conversion. *Breast Cancer Res* **3,** 213–217.
[23] De Wever O and Mareel M (2003). Role of tissue stroma in cancer cell invasion. *J Pathol* **200,** 429–447.
[24] Thiery JP (2002). Epithelial–mesenchymal transitions in tumor progression. *Nat Rev Cancer* **2,** 442–454.
[25] Daldrup H, Shames DM, Wendland M, Okuhata Y, Link TM, Rosenau W, Lu Y, and Brasch RC (1998). Correlation of dynamic contrast-enhanced magnetic resonance imaging with histologic tumor grade: comparison of macromolecular and small-molecular contrast media. *Pediatr Radiol* **28,** 67–78.
[26] Haase A, Matthaei D, Bartkowski R, Duhmke E, and Leibfritz D (1989). Inversion recovery snapshot FLASH MR imaging. *J Comput Assist Tomogr* **13,** 1036–1040.
[27] Galiè M, D'Onofrio M, Calderan L, Nicolato E, Amici A, Crescimanno C, Marzola P, and Sbarbati A (2004). *In vivo* mapping of spontaneous mammary tumors in transgenic mice using MRI and ultrasonography. *J Magn Res Imaging* **19,** 570–579.
[28] Marzola P, Farace P, Calderan L, Crescimanno C, Lunati E, Nicolato E, Benati D, Degrassi A, Terron A, Klapwijk J, et al. (2003). *In vivo* mapping of fractional plasma volume (fPV) and endothelial transfer coefficient (kPS) in solid tumors using a macromolecular contrast agent: correlation with histology and ultrastructure. *Int J Cancer* **104,** 462–468.
[29] Netti PA, Roberge S, Boucher Y, Baxter LT, and Jain RK (1996). Effect of transvascular fluid exchange on pressure–flow relationship in tumors: a proposed mechanism for tumor blood flow heterogeneity. *Microvasc Res* **52,** 27–46.
[30] Hobson B and Denekamp J (1984). Endothelial proliferation in tumours and normal tissues: continuous labelling studies. *Br J Cancer* **49,** 405–413.
[31] Denekamp J and Hobson B (1982). Endothelial-cell proliferation in experimental tumors. *Br J Cancer* **46,** 711–720.
[32] Rak JW, St Croix BD, and Kerbel RS (1995). Consequences of angiogenesis for tumor progression, metastasis and cancer therapy. *Anticancer Drugs* **6,** 3–18.
[33] Kinouchi M, Mano M, Matsuoka I, Kodama S, Aoki T, Okamoto M, Yamamura H, Usami M, and Takahashi K (2003). Immature tumor angiogenesis in high-grade and high-stage renal cell carcinoma. *Urology* **62,** 765–770.
[34] Less JR, Skalak TC, Sevick EM, and Jain RK (1991). Microvascular architecture in a mammary carcinoma: branching patterns and vessel dimension. *Cancer Res* **51,** 265–273.
[35] Thiery JP (2002). Epithelial–mesenchymal transition in tumor progression. *Nat Rev Cancer* **2,** 442–454.